Evaluation of the Temperature Margin of a Conduction-Cooled Superconducting Magnet Package for the ILC Main Linac

Ó. Durán, L. García-Tabarés, L. A. González, F. Toral, Y. Arimoto, T. Yamada, A. Yamamoto, T. Boutboul, J. Fleiter, S. C. Hopkins, and J. C. Pérez

***Abstract*—The Main Linac of the International Linear Collider (ILC) includes one superconducting quadrupole (SCQ) package within each of the Type-B cryomodules. This combined-function, superconducting magnet focuses and steers the electrons and positrons. Due to magnet assembly constraints, it must be splittable, and therefore cryogen-free, that is, conductively cooled via thermal links. Additionally, a large pulsed heat deposition is expected in the superconducting coils due to beam-induced dark currents. As an alternative to the Nb-Ti magnet developed by KEK, CIEMAT explores a proposal based on bronze-route Nb_3Sn that withstands the dark current heat loads by profiting from the higher thermal margin of the superconductor. This paper reports the thermal analysis on the magnet design to maximize the temperature margin provided by the Nb_3Sn technology. The selected wire was measured to define its critical surface at the atypical low field and low current operation region of the SCQ of ILC. The operation temperature profile of the coil was examined with analytical and finite element models, including a thorough examination on the anisotropic behaviour of the impregnated Nb_3Sn quadrupole coils. A highly conductive casing for the coil was designed and high purity aluminum sheets were integrated to significantly improve the thermal management via dry cooling.**

***Index Terms*—ILC, conduction cooling, splittable superconducting quadrupole package, temperature margin.**

I. Introduction

THE International Linear Collider (ILC) is a candidate for a future large-scale electron-positron collider [1]. Niobium superconducting (SC) RF cavities are integrated into two types of cryomodules to form the main linac. In the Type-B cryomodule, integrated with eight cavities, a SC quadrupole package (SCQ) provides focusing plus vertical and horizontal steering. After the cavity-string assembly in the clean room, the splittable magnet is assembled around the beam pipe. The magnet is cooled by conduction from the outer surface of the transfer line supplying He to the cavities.

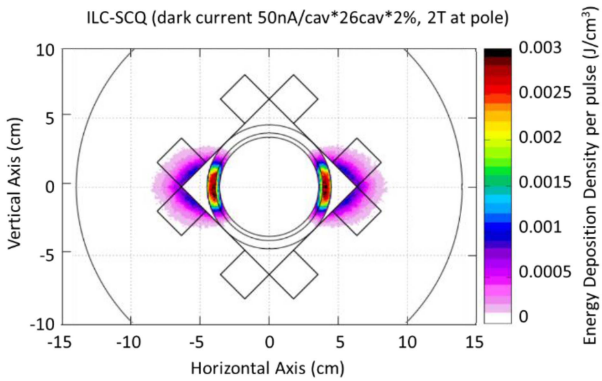

Fig. 1. Dark current heat deposition profile [2].

A model magnet developed by Fermilab and KEK [3], [4] was tested both in liquid bath and in conduction cooling configuration [3], [5], [6]. A shorter model magnet was integrated and energized in a cryomodule at the Superconducting Test Facility at KEK [7].

In that design, a risk of quench of the Nb-Ti coils was found ascribed to the field-emission electrons, so-called dark currents, initiated at high electric field locations in the SRF cavities [8]. In the ILC, these electrons may travel in parallel to the main beam and are strongly deflected by the quadrupole field. Consequently, the dark current deposits energy in the divergence plane, reaching the coils (Fig. 1) [2]. The heat load was estimated to reach up to 5 W for a 500 GeV ILC, including a safety factor of more than 3. This would raise the coil temperature beyond 7 K - the critical temperature of Nb-Ti at 3 T - within a few pulses (< 0.5 sec) [9]. To mitigate this risk, KEK develops currently a magnet with absorbers that intercept and extract the heat before it reaches the Nb-Ti coils [10].

In parallel, CIEMAT investigates an alternative SCQ package design [11], where the dark-current heat load is absorbed by the superconducting magnet section without the need for interception. The requirement for a high thermal margin excluded the use of Nb-Ti, leading to the selection of bronze-route Nb_3Sn

Received 13 October 2025; revised 14 January 2026; accepted 17 February 2026. Date of publication 9 March 2026; date of current version 19 March 2026. This work was supported by the Spanish Ministry of Science, Innovation and Universities through 2020 R&D Program under Project PID2020-120582GB-I00. *(Corresponding author: Ó. Durán)*

Ó. Durán is with the Centro de Investigaciones Energéticas, Medioambientales y Tecnológicas (CIEMAT), 28040 Madrid, Spain, and also with the Higher Technical School of Industrial Engineering, Madrid Polytechnical University, 28006 Madrid, Spain (e-mail: oscar.duran@ciemat.es).

L. García-Tabarés, L. A. González, and F. Toral are with CIEMAT, 28040 Madrid, Spain (e-mail: fernando.toral@ciemat.es).

Y. Arimoto, T. Yamada, and A. Yamamoto are with the High Energy Accelerator Research Organization KEK, Tsukuba 305-0801, Japan.

T. Boutboul, J. Fleiter, S. C. Hopkins, and J. C. Pérez are with CERN, 1211 Geneva, Switzerland.

Color versions of one or more figures in this article are available at https://doi.org/10.1109/TASC.2026.3670790.

Digital Object Identifier 10.1109/TASC.2026.3670790

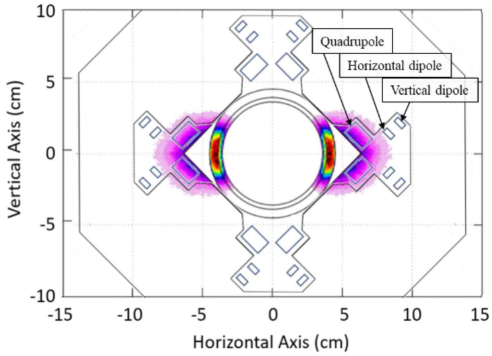

Fig. 2. Proposed magnet cross-section [11] with superposed heat profile from estimations of Fig. 1 [2].

for the quadrupole coils after extensive evaluation of conductors and requirements of this magnet. Due to the small space for the splices on the leads, the quadrupole and dipole coils were split. In the proposed electromagnetic design for the high energy version of the magnet, the dark-current heat deposition profile does not reach the separated dipoles (Fig. 2), enabling the selection of Nb-Ti as wire for the dipole coils [11].

II. Conductor Characterization

The design of Nb_3Sn wire layouts, especially internal-tin and powder-in-tube techniques, is commonly oriented towards high magnetic fields and large transport currents at low temperatures [12]. Typical wire measurements campaigns are conducted at a liquid Helium bath at 4.2 K and magnetic fields starting from 10 T. Studies focusing on low-field and high-temperature behavior exist [13] but remain scarce due to constraints imposed by power converters [14] and the limited practical applicability of these operating conditions. To investigate the performance of the selected HNST-0.6 mm bronze-route Nb_3Sn wire from Supercon [15] within the magnet requirements [11], a characterization campaign was conducted at CERN.

The wire diameter was measured with high precision before and after the heat treatment using a laser micrometer. The measured increase of 0.3 % is small compared to the reference high-Jc manufacturing techniques [16]. This wire expansion can be absorbed by the 0.75 mm thick S2-glass fiber wire insulation, enabling the use of nominal coil dimensions in the reaction tooling design.

The critical transport current was measured at 4.2 K and external fields from 1 T to 12 T with high current power supplies. The results are consistent with the specifications provided by the manufacturer, Supercon Inc. [15], confirming the repeatability of both the heat treatment and the performance of the wire. Self-field corrections were applied to evaluate the wire at its peak field, and the measured transport critical curve was expanded towards low field.

Magnetization measurements with Vibrating-Sample Magnetometry (VSM) were also conducted at temperatures from 1.9 K to 16 K (Fig. 3). The wire presented smooth magnetization curves even at low temperatures, predicting a good stability against flux jumps. The amplitude of the magnetization loops is consistent with ITER bronze-route wires of similar

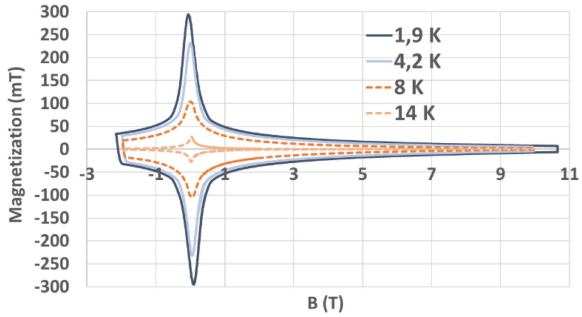

Fig. 3. Magnetization measurements at different temperatures.

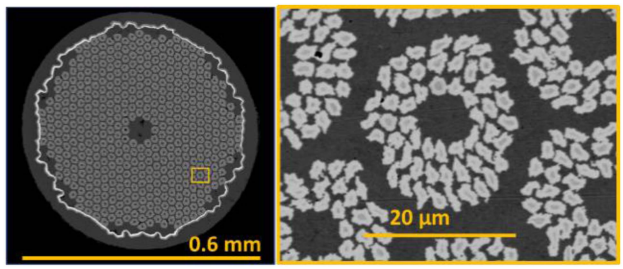

Fig. 4. Optical micrographs of the reacted HNST-0.6 mm.

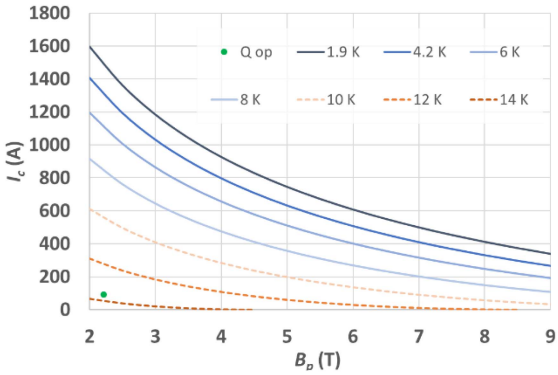

Fig. 5. Extrapolated critical surface for bronze-route Nb_3Sn 0.6 mm Supercon HNST wire for fields inside the region $0.1<b<0.7$.

characteristics [17], and the fitting equations revealed an effective filament diameter (d_{eff}) of 21 μm.

Optical micrographs were also performed on the wire (Fig. 4). The A15 layer is visible in light gray surrounding the unreacted Nb. EDX analysis confirmed the good reaction via low residual Sn content of the Cu-Sn matrix. Partial filament contacts are visible, forming clearly isolated sub-bundles of about 20 μm, consistent with the measured magnetization behavior.

Magnetization and transport current data share a $b^p(1\text{-}b)^q$ dependence on reduced field b according to scaling laws [18]. This allows a combination of the presented transport current measurements at 4.2 K and the magnetization measurements at different temperatures to construct the critical current surface of the wire [19]. Excellent agreement with this scaling is achievable for $0.1 < b < 0.7$, while deviations occur at the low and high extremes of the field. Fig. 5 presents the critical surface of the

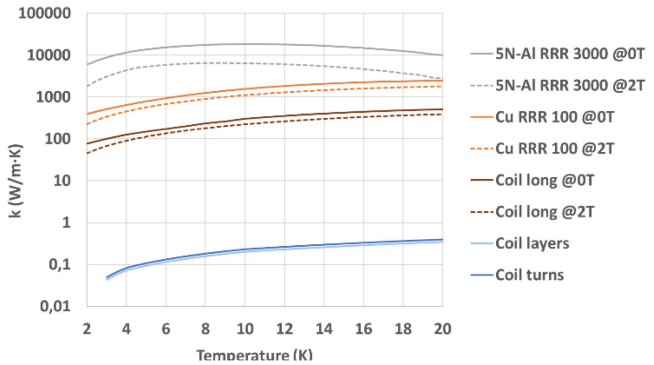

Fig. 6. Thermal conductivity of the materials used in the models.

wire, extrapolated from fields above 2 T up to 9 T. The most demanding operating point of the quadrupole coil, according to the electromagnetic calculations [11], is also represented by a green point. The extrapolation indicates a minimum critical temperature of 13.5 K for superconductor under the quadrupole coil requirements in field and current.

III. Thermal Analysis

Provided the critical temperature of the superconductor, the determination of the temperature margin requires calculating the maximum temperature reached by the coil under the most demanding thermal loading due to dark-current heating.

The thermal load is caused by the pulsed dark-current electrons associated to the beam, with a bunch every 0.2 s (5 Hz). The impacting electrons of a bunch deposit 1 J within 1 ms into the magnet [2], equally distributed in the four coils due to symmetry (Fig. 1). In each coil, the straight-section leg located in the focusing plane receives no heat input, while in the defocusing plane, only the downstream half of the leg is heated, as required by the longitudinal space needed for the electrons to bend. Besides, the electrons deposit the main energy fraction into the closest half of the cross-section [2].

The racetrack coils are cooled from the longitudinal end via conduction. Highly conductive materials extract the heat from the coil center to the longitudinal ends, where the heat is further evacuated via high purity aluminum sheets that are anchored to the exterior of a transfer line providing 2 K liquid helium to the cavities. The reaction process and the brittle nature of Nb_3Sn require the use of epoxy impregnated S2-glass fiber insulation, complicating the transversal extraction of the heat due to the low thermal conductivity of the resin. To evaluate this limitation, the thermal paths were modeled with an increasing level of detail to better understand the heat transfer mechanisms, improve the cooling performance, and maximize the available thermal margin.

A. Static Analytical Analysis

In a first step, a conservative thermal resistive analytical model was developed. The layout of the impregnated coil cross-section implies anisotropy in the thermal material properties and requires the modelling of three different parallel paths for the longitudinal heat extraction: (i) the copper in the conductor matrix, (ii) the external copper casing, and (iii) the external aluminum sheets. The magnetoresistance effects in copper and aluminum were included (Fig. 6), and all the properties were evaluated at a conservative magnetic field of 2 T [20]. Longitudinally, the resin was assumed to transfer negligible heat. In the cross-sectional plane, the heat must pass through the low-conductivity epoxy layers before reaching the outer surface, where the high-conductivity elements are connected in series in the model. The internal transverse coil conductivity was extrapolated to this coil layout from experimentally measured data of similar coil configurations [21].

Based on these considerations, the model establishes a total equivalent thermal resistance (R_{eq}) of 3.9 K·W^{-1}. The pulsed heat input was simplified to a continuous heat input to compute the steady-state temperature. With five bunches of 1 J per second distributed across the four coils, the heat load per coil ($\ddot{Q}$) is 1.25 W. As a conservative boundary condition, all the heat is assumed to flow to the nearest coil end ($T_{cold\ sink}$), which is assumed at 4 K. Applying the thermal conduction (1), a maximum temperature of 8.9 K was obtained as a reference value for these conservative assumptions.

$$\dot{Q} = \left(T_{\max} - T_{cold\ sink}\right) / R_{eq} \tag{1}$$

The model revealed that the through-coil transverse conductivity constitutes the primary bottleneck in the overall heat-conduction path. Increasing the thickness of the surrounding components has little effect on the equivalent resistance, since their high thermal conductivity k_m keeps their resistance very low. According to the conduction resistance (2), compact coil configurations improve cooling performance by reducing the quantity of resin layers hence the path length L. To that end, the electromagnetic design and current limitation to 100 A indicated that the coils should be positioned as close as possible to both the aperture and the yoke for optimal efficiency [11]. Consequently, the oxygen-free Cu casing thickness was reduced to 2 mm and the aluminum sheet to 0.5 mm. Although the coil efficiency is reduced by the presence of the upper aluminum sheet, the contribution of this thermal path remains essential. The maximum temperature estimated without Al sheets is 12.4 K.

$$R = L \,/\, (A * k_m) \tag{2}$$

The heat-path analysis indicated that the aluminum sheets account for half of the total heat extraction, benefiting from their proximity to the heat source. The copper casing removes one third of the total heat, with its effectiveness reduced by its larger distance from the deposition area. The wire path contributes the least, since once extracted internally to the longitudinal end, the heat must still propagate across the coil head cross-section to reach the cold sink.

B. Steady-State FEM Analysis

The analytical model has limitations by its assumption that the thermal paths are only parallel, whereas in reality they are also interconnected in each cross-section slice. Furthermore, the heat is also conducted through the cold leg, although that path is of lower influence due to its greater length. To improve the accuracy of the calculations and capture the 3-D effects, a finite element model (FEM) was built in ANSYS [22] (Fig. 7). The same thermal properties and the anisotropy of the coil described in the

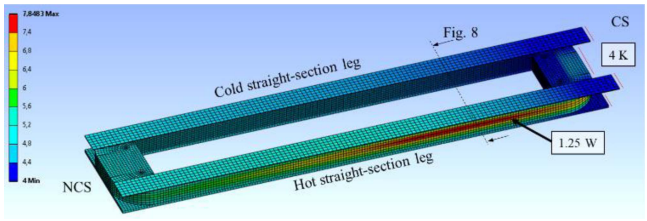

Fig. 7. Coil temperature distribution.

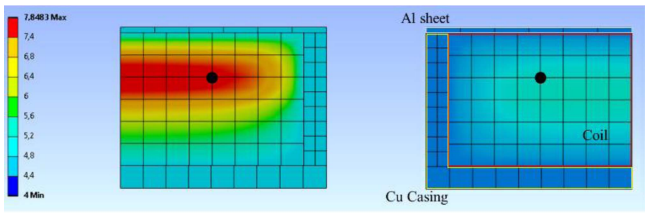

Fig. 8. Cross-section temperature distribution at worst longitudinal position. Left: hot leg; right: cold leg.

analytical mode were also implemented here. The heat load was modeled as a uniform internal heat deposition of 1.25 W over the upper volume of one half-leg. The FEM results were consistent with the analytical predictions and provided a maximum temperature of 7.7 K, in the same location (Fig. 8) identified by the analytical model. The high efficiency of the longitudinal heat extraction is evidenced by the small temperature gradients along the coil (Fig. 7). However, the anisotropy of the coil and the low thermal conductivity of the resin become clearly appreciable in the temperature distribution of the coil legs (Fig. 8). The largest temperature gradient occurs in the left hot leg, while the heat is transferred to the upper half of the cold leg via the highly conductive wires.

The static analysis highlights the influence of the thermal conductivity on the coil performance. Only by improving the resin conductivity can the steady-state temperature be further reduced. Although alumina-filled epoxy would enhance thermal conduction, it presents challenges for the vacuum impregnation in a coil whose glass fiber insulation has already undergone the Nb_3Sn reaction heat treatment. At this stage, it is not included in the baseline design.

C. Time Transient Analysis

The steady-state analysis exposed the location of the hot spot in the coil, but did not consider the complexity provided by the pulsed heat input associated with the beam bunches. Each coil receives 0.25 J within 1 ms. During the 0.2 s interval between bunches, the heat is partially extracted and transmitted throughout the coil via conduction, while a fraction is accumulated into the heat capacity of the coil materials.

Due to the strong influence of the 3D effects, evaluating the transient response analytically is impractical. Therefore, the FEM model explained above was employed to simulate the time-dependent heat load. The temperature-dependent specific heat capacities (Cp) from CryoComp [20] were assumed isotropic for all the materials, and the overall coil Cp was obtained as a mass-weighted average of its constituents. The resin, with its

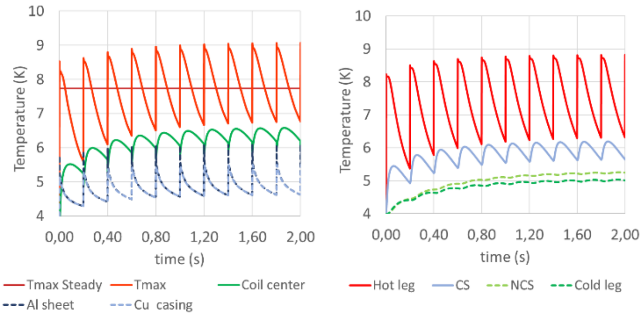

Fig. 9. Left: evolution of the hottest cross-section. Right: evolution in a same turn depending on coil position.

relatively high Cp, represents the primary stabilizing element. The bronze matrix and the Nb_3Sn stay as following contributions, while copper provides the smallest effect due to both its low mass fraction and Cp.

Fig. 9 (left) shows the temperature evolution of the hottest cross-section (Fig. 8). The transient simulation indicates a peak maximum temperature of 9 K, which corresponds to 4.5 K of temperature margin relative to the 13.5 K critical temperature of the superconductor. After a few beam pulses, the system reaches a stable periodic regime in which the temperature oscillates around the steady-state value. The external copper and aluminum components exhibit fast thermal transients due to their lower Cp. However, the coil does not reach a homogeneous temperature between bunches, neither within the cross-section nor in different positions along the coil winding. To evaluate the latter, a wire turn, marked with a black dot in Fig. 8, was monitored in both coil legs and heads. Fig. 9 (right) shows that the cold leg remains thermally stable, while the connection side (CS) exhibits attenuated fluctuations due to the heat-capacity damping along the conduction path from the heat source in the hot leg.

A FEM model was prepared to support and guide the experimental validation of the Nb_3Sn test coil, reproducing the controlled heat input from surface heaters and the temperature mapping along the coil. It will enable direct comparison and validation of the analytical predictions and material properties assumptions once the experimental results are obtained.

IV. Conclusion

The presented Nb_3Sn coil design provides a minimum temperature margin of 4.5 K. The conductor properties were characterized and the operation temperatures of the coil were thoroughly analyzed. Analytical and finite element models offer a complete and complementary understanding of the coil assembly heat transfer.

At CIEMAT, the Nb3Sn quadrupole test coil will be manufactured and tested in mirror configuration via conduction cooling in a cryocooler test facility to validate the models, design, materials and manufacturing processes.

Acknowledgment

The authors warmly thank David Frost (Supercon Inc) for the Nb_3Sn wire information and samples for characterization.

REFERENCES

[1] C. Adolphsen, "The international linear collider technical design report - volume 3.II: Accelerator baseline design," ILC-REPORT-2013-040, 137940, Jun. 2013, *arXiv:1306.6328*.

[2] A. Yamamoto and N. Solyak, "Dark current electrons and irradiation heating of superconducting magnets for high-gradient SRF linacs," presented at the TESLA Technol. Collaboration (TTC'21), DESY, Hamburg, Germany, 2021.

[3] V. S. Kashikhin et al., "Superconducting splittable quadrupole magnet for linear accelerators," *IEEE Trans. Appl. Supercond.*, vol. 22, no. 3, Jun. 2012, Art. no. 4002904, doi: 10.1109/TASC.2011.2176297.

[4] V. Kashikhin et al., "Performance of conduction cooled splittable superconducting magnet package for linear accelerators," *IEEE Trans. Appl. Supercond.*, vol. 26, no. 4, Jun. 2016, Art. no. 4103405, doi: 10.1109/TASC.2016.2532365.

[5] N. Andreev et al., "Conduction cooling test of a splittable quadrupole for ILC cryomodules," *IEEE Trans. Appl. Supercond.*, vol. 23, no. 3, Jun. 2013, Art. no. 3500305, doi: 10.1109/TASC.2012.2236135.

[6] N. Kimura et al., "Cryogenic performance of a conduction-cooling splittable quadrupole magnet for ILC cryomodules," in *AIP Conf. Proc.*, vol. 1573, 2014, pp. 407–415, doi: 10.1063/1.4860730.

[7] H. Shimizu et al., "Study on conduction cooling of superconducting magnets for the ILC main linac," *IEEE Trans. Appl. Supercond.*, vol. 32, no. 6, Sep. 2022, Art. no. 4002805, doi: 10.1109/TASC.2022.3155487.

[8] A. I. Sukhanov et al., "Dark current studies in ILC main linac," in *28th Int. Linear Accel. Conf.*, 2017, Art. no. THPLR007, doi: 10.18429/JACoW-LINAC2016-THPLR007.

[9] Y. Arimoto et al., "Design study of a superconducting quadrupole magnet system sustainable under dark current heating in ILC main linac," *IEEE Trans. Appl. Supercond.*, vol. 33, no. 5, Aug. 2023, Art. no. 4002104, doi: 10.1109/TASC.2023.3252484.

[10] T. Yamada et al., "Development status of a NbTi conduction-cooled superconducting quadrupole magnet combined with dipole correctors for the ILC main linac," presented at the ICEC29/ICMC2024, Geneva, Switzerland, Jul. 24, 2024, Poster. [Online]. Available: https://indico.cern.ch/event/1296489/contributions/5882011/

[11] Ó. Durán et al., "Conceptual design of a conduction-cooled superconducting quadrupole for ILC main linac with large temperature margin," *IEEE Trans. Appl. Supercond.*, vol. 35, no. 5, Aug. 2025, Art. no. 4003605, doi: 10.1109/TASC.2025.3549412.

[12] A. Ballarino et al., "The CERN FCC conductor development program: A worldwide effort for the future generation of high-field magnets," *IEEE Trans. Appl. Supercond.*, vol. 29, no. 5, Aug. 2019, Art. no. 6001709, doi: 10.1109/TASC.2019.2896469.

[13] L. F. Goodrich and T. C. Stauffer, "Variable-temperature critical-current measurements on a Nb_3Sn wire," *IEEE Trans. Appl Supercond.*, vol. 15, no. 2, pp. 3356–3359, Jun. 2005, doi: 10.1109/TASC.2005.848902.

[14] E. Barzi et al., "Instabilities in transport current measurements of Nb_3Sn strands," *IEEE Trans. Appl Supercond.*, vol. 15, no. 2, pp. 3364–3367, Jun. 2005, doi: 10.1109/TASC.2005.848906.

[15] "Nb_3Sn superconducting wires | supercon inc.," Accessed: Sep. 13, 2024, [Online]. Available: https://www.supercon-wire.com/content/nb3sn-superconducting-wires

[16] C. Scheuerlein et al., "Effect of the fabrication route on the phase and volume changes during the reaction heat treatment of Nb_3Sn superconducting wires," *Supercond. Sci. Technol.*, vol. 33, no. 3, Mar. 2020, Art. no. 034004, doi: 10.1088/1361-6668/ab627c.

[17] B. Bordini et al., "Magnetization and inter-filament contact in HEP and ITER bronze-route Nb_3Sn wires," *IEEE Trans. Appl. Supercond.*, vol. 21, no. 3, pp. 3373–3376, Jun. 2011, doi: 10.1109/TASC.2010.2092733.

[18] J. W. Ekin, "Unified scaling law for flux pinning in practical superconductors: I. Separability postulate, raw scaling data and parameterization at moderate strains," *Supercond. Sci. Technol.*, vol. 23, no. 8, Aug. 2010, Art. no. 083001, doi: 10.1088/0953-2048/23/8/083001.

[19] S. C. Hopkins et al., "Critical current scaling of Nb_3Sn wires over an extended field range combining magnetisation and transport data," presented at the EUCAS2025, Oporto, Portugal, Sep. 22, 2025, Oral presentation. [Online]. Available: https://eucas2025.abstractserver.com/program/#/details/presentations/763

[20] CryoComp, v.5.3, Eckels Engineering Inc., 3322 Ebenezer Chase Drive Florence SC 29501-8006 USA, 2017.

[21] T. Koettig et al., "Thermal conductivity measurements of impregnated Nb_3Sn coil samples in the temperature range of 3.5 K to 100 K," in *IOP Conf. Ser. Mater. Sci. Eng.*, vol. 171, 2017, Art. no. 012103, doi: 10.1088/1757-899X/171/1/012103.

[22] AnsysWorkbench, Release 2023R1. Ansys Inc., (n.d.), 2023. [Online]. Available: www.ansys.com